



# Scalable and eco-friendly production of flexible, hierarchical porous MXene/polyimide composites with superior electromagnetic interference shielding

Na Gyung Kim<sup>a,b,1</sup>, Jeong Min Jang<sup>b,e,1</sup>, Young-Jun Kim<sup>a,1</sup>, Ju Yeon Kim<sup>b</sup>, Donghyeon Kang<sup>c,d</sup>, Jongmin Park<sup>a</sup>, Jong Chan Won<sup>a,f</sup>, Sang-Woo Kim<sup>c,d</sup>, Dae Woo Kim<sup>b,\*</sup>, Seon Joon Kim<sup>e,g,\*\*</sup>, Yun Ho Kim<sup>a,f,\*\*\*</sup>

<sup>a</sup> Advanced Functional Polymers Research Center, KRICT, Daejeon, Republic of Korea

<sup>b</sup> Department of Chemical and Biomolecular Engineering, Yonsei University, Seoul, Republic of Korea

<sup>c</sup> Center for Human-oriented Triboelectric Energy Harvesting, Yonsei University, Seoul, Republic of Korea

<sup>d</sup> Department of Materials Science and Engineering, Yonsei University, Seoul, Republic of Korea

<sup>e</sup> Convergence Research Center for Solutions to Electromagnetic Interference in Future-mobility and Extreme Materials Research Center, KIST, Seoul, Republic of Korea

<sup>f</sup> Advanced Materials and Chemical Engineering, KRICT School, University of Science and Technology, Daejeon, Republic of Korea

<sup>g</sup> Division of Nanoscience and Technology, KIST School, University of Science and Technology, Seoul, Republic of Korea

## ARTICLE INFO

### Keywords:

Electromagnetic interference shielding  
Water-borne polyimide  
MXene composite  
Porous structure  
MXene dispersion

## ABSTRACT

MXene-based composites are widely recognized for their exceptional electromagnetic interference (EMI) shielding capabilities. While incorporating porous structures can enhance shielding efficiency, achieving scalable and uniformly distributed porosity remains a significant challenge. Here, we report the fabrication of large-area, flexible, and porous MXene/polyimide (PI) composite films using a water-borne polyimide (W-PI) matrix and polycarboxylate ether (PCE)-functionalized  $\text{Ti}_3\text{C}_2\text{T}_x$  MXene. The comb-like structure of PCE ensures uniform MXene dispersion, while its branched functional groups promote the formation of macro pores during thermal imidization. As a result, the composites exhibit outstanding EMI shielding effectiveness, reaching 66.1 dB in the X-band and 85.0 dB in the Ka-band. The porous architecture, generated through PCE evaporation and MXene thermal expansion, enhances both reflection and absorption pathways, further improving shielding performance. Additionally, the films demonstrate high electrical conductivity, exceptional flexibility with bending radii below 2 mm, and remarkable durability, retaining over 95 % of their shielding efficiency after 1000 bending cycles. This eco-friendly, water-borne processing strategy, combined with scalable slot-die coating, highlights the immense potential of these composites for next-generation applications in 5G communications, wearable electronics, and flexible devices.

## 1. Introduction

The rapid advancement of electronic and communication technologies has intensified the demand for effective electromagnetic interference (EMI) shielding materials to ensure signal integrity and minimize electromagnetic disturbances [1–6]. Traditional metal-based shielding materials, while highly conductive, suffer from limitations such as high

density, corrosion susceptibility, and lack of flexibility, making them unsuitable for modern lightweight and adaptable applications [7–11]. In contrast, polymer-based composites have emerged as promising alternatives due to their low density, flexibility, and ease of processing, particularly when combined with advanced conductive fillers. Achieving high electrical conductivity is critical for EMI shielding performance, making the selection of highly conductive fillers essential.

\* Corresponding author.

\*\* Corresponding author. Convergence Research Center for Solutions to Electromagnetic Interference in Future-mobility and Extreme Materials Research Center, KIST, Seoul, Republic of Korea.

\*\*\* Corresponding author. Advanced Functional Polymers Research Center, KRICT, Daejeon, Republic of Korea.

E-mail addresses: [audw1105@yonsei.ac.kr](mailto:audw1105@yonsei.ac.kr) (D.W. Kim), [seonjkim@kist.re.kr](mailto:seonjkim@kist.re.kr) (S.J. Kim), [yunho@kRICT.re.kr](mailto:yunho@kRICT.re.kr) (Y.H. Kim).

<sup>1</sup> These authors contributed equally.

Among various fillers, MXenes have demonstrated exceptional potential for EMI shielding applications, with  $\text{Ti}_3\text{C}_2\text{T}_x$  MXene standing out due to its superior electrical conductivity [12–16]. Additionally, the densely populated functional groups and tunable surface chemistry of MXenes enhance their versatility for polymer composite synthesis. The hydrophilic nature of as-synthesized MXenes, attributed to surface functional groups such as  $-\text{OH}$  and  $-\text{O}$ , allows for excellent dispersion in water. This property enables their seamless integration with water-soluble polymers such as poly(acrylic acid) (PAA) and poly(vinyl alcohol) (PVA), facilitating eco-friendly processing techniques. Furthermore, the two-dimensional morphology and high surface area of MXene sheets promote the formation of robust conductive networks within polymer matrices, which are crucial for achieving high EMI shielding performance [17–19].

However, simply incorporating MXene into polymer composites often fails to achieve the electrical conductivity necessary for optimal EMI shielding. The MXene filler content is typically constrained, as excessive loading can compromise the structural stability and mechanical integrity of the composite. To overcome this limitation, additional EMI shielding mechanisms must be employed. One effective approach involves introducing pores to enhance wave attenuation through internal reflection and multiple scattering. Various methods, such as rapid annealing of MXenes or the incorporation of sacrificial polymer beads, have been explored to create porous structures. Nevertheless, achieving a uniform and dense pore distribution while maintaining structural and mechanical integrity remains a significant challenge, particularly in large-area, high-MXene-content polymer composites. Additionally, developing a fabrication method compatible with scalable polymer processing techniques is essential for practical applications.

In this study, we present a scalable and eco-friendly approach for fabricating MXene/polyimide composites with hierarchical porous structures and enhanced EMI shielding performance. We address previous challenges by utilizing comb-type polycarboxylate ether (PCE) as a dual-function additive: (1) as a dispersing agent to improve the solubility and uniform distribution of MXene sheets within the polymer matrix and (2) as a porogen to facilitate the formation of hierarchical porous structures during thermal imidization. The use of PCE ensures stable MXene dispersion within water-borne poly(amic acid) salt (W-PAAS) matrices, a key step for scalable and environmentally friendly fabrication. Additionally, water-borne polyimide (PI) [20–25] provides advantages such as reduced environmental impact and compatibility with hydrophilic fillers like MXene, making them ideal for high-performance EMI shielding composites. Furthermore, the integration of a water-borne polymer system with a fully aqueous MXene dispersion significantly reduces the need for organic solvents, meeting growing demands for environmentally responsible EMI shielding materials. The slot-die coating process adopted in this study is also compatible with large-scale industrial production, offering practical advantages over conventional lab-scale fabrication techniques. By utilizing PCE evaporation and the thermal expansion of MXene during imidization, this study achieves large-area, high-MXene-content polymer composites with well-defined porous architectures. These structures significantly enhance EMI shielding by increasing wave absorption, promoting multiple reflection and scattering pathways, and preserving the mechanical flexibility and structural integrity of the films.

## 2. Experimental section

### 2.1. Materials

3,3',4,4'-Biphenyltetracarboxylic dianhydride (BPDA) and *p*-phenylenediamine (pPDA) were purchased from Sunlight Chemical, China, and dried in a vacuum oven at 200 °C and 70 °C, respectively, for 6 h before use. 1,2-Dimethylimidazole (DMIZ) was obtained from Sigma-Aldrich and used without further purification. A polycarboxylate ether polymer aqueous solution was sourced from L'BESTE GAT and dried at 25 °C

for approximately 2 days in a vacuum oven before use.

### 2.2. Synthesis of $\text{Ti}_3\text{C}_2\text{T}_x$ MXene nanosheets

To prepare the etching solution, 20 mL of 9 M HCl was placed in a polypropylene bottle, and 1.6 g of LiF was added under stirring at 35 °C until fully dissolved as following MILD method [26]. Subsequently, 1 g of  $\text{Ti}_3\text{AlC}_2$  powder was gradually introduced into the etching solution and left to react at 35 °C for 24 h. The resulting solution, containing etched multilayer  $\text{Ti}_3\text{C}_2\text{T}_x$  MXene and partially etched  $\text{Ti}_3\text{AlC}_2$ , was centrifuged at 5000 rpm for 5 min. The acidic supernatant was discarded, and the sediment was washed with deionized water to remove residual LiF/HCl etchants. This washing process was repeated until the pH of the supernatant approached neutrality. The solution was then vigorously shaken to delaminate  $\text{Ti}_3\text{C}_2\text{T}_x$  MXene into single sheets. Finally, the delaminated sheets were separated by centrifugation at 3500 rpm for over 30 min, and the supernatant containing the delaminated MXene sheets was collected for further use.

### 2.3. Synthesis of water-borne poly(amic acid) salts

Water-borne poly(amic acid) salts (W-PAAS) were synthesized using previously reported methods [24,25]. Specifically, BPDA/pPDA-based W-PAAS was prepared via a one-step polymerization process conducted in an aqueous solution with 1,2-dimethylimidazole (DMIZ) as an organic base to facilitate salt formation [25]. The reaction was carried out in a three-necked flask equipped with a mechanical stirrer under a nitrogen atmosphere to prevent oxidation. For the synthesis, DMIZ (200 mmol) and pPDA (80 mmol) were dissolved in deionized (DI) water (753.3 mL) and stirred at 25 °C for 1 h to ensure complete dissolution. Subsequently, BPDA (80 mmol) was gradually added to the solution, and the reaction mixture was stirred at 70 °C for 18 h. This process resulted in the formation of a viscous aqueous solution of W-PAAS with a concentration of 6.8 wt%, which was prepared for subsequent processing steps.

### 2.4. Preparation of PCE- $\text{Ti}_3\text{C}_2\text{T}_x$ MXene/PI composite films

The PCE- $\text{Ti}_3\text{C}_2\text{T}_x$  MXene/PI (PM-XX) composite films were prepared through a sequential process involving mixing, solution casting, and thermal imidization. Initially, PCE was added to a water-dispersed MXene solution (30 mg mL<sup>-1</sup>) at a concentration of 43 wt% relative to the MXene solid content. This value was determined by excluding the mass of water and other volatile components from the total weight, which aligns with previous studies using a similar basis for surfactant-to-MXene ratios in emulsion systems [27]. The mixture was vigorously stirred at 2000 rpm for 20 min using a revolutionary mixer (ARE-310, THINKY). Subsequently, W-PAAS solution was added to the PCE-treated MXene under continuous agitation. The resulting solution was again mixed at 2000 rpm for 5 min using the same mixer. Composite films (PM-XX) were then fabricated using a slot-die coater (Table Slot Die Coater, DCN Co., Ltd). The films underwent a stepwise thermal imidization process to achieve their final form. The imidization involved sequential heating in a vacuum oven at 50, 80, 100, and 120 °C, followed by hot pressing at 150, 200, and 250 °C, and final heating at 300, 350, and 380 °C, with each step maintained for 40 min. The mass ratios of MXene to PI were varied as 7:3, 5:5, 3:7, and 1:9, corresponding to composite films designated as PM-30, PM-50, PM-70, and PM-90, respectively. The final film thicknesses were measured to be 41.5 μm, 45.3 μm, 37.2 μm, and 32 μm for PM-30, PM-50, PM-70, and PM-90, respectively.

### 2.5. Characterization

A residual solvent signal was used as an internal standard to obtain the <sup>1</sup>H nuclear magnetic resonance (<sup>1</sup>H NMR) spectra using a Bruker

advance 500 MHz spectrometer (Billerica, MA, USA). Size exclusion chromatography (SEC) was conducted in N-methyl-2-pyrrolidinone (NMP) solution with 0.02 M of  $\text{H}_3\text{PO}_4$  and 0.02 M of LiBr at 50 °C with a flow rate of 0.8 mL/min on the Shodex (Showa Denko, Minato, Japan). The instrument was equipped with three poly(hydroxy methacrylate) columns (multi-pore) with a molar mass of 200–20,000,000 g/mol. Fourier transform infrared (FT-IR) spectra were obtained using Bruker Alpha-P spectrophotometer in the range of 650–4000  $\text{cm}^{-1}$  under ambient conditions. All rheological tests were conducted using a modular compact rheometer (MCR 302e, Anton Paar, Austria) at 25 °C with a plate-plate geometry. The spindle diameter was 25 mm and the gap between plates was 1 mm. Measurements were conducted immediately after the mixing process of the samples. Prior to all measurement runs, the inserted samples were exposed to a 5-min equilibrium period to ensure the correct temperature of the samples and an acceptable level of the residual normal force. Steady flow curves and deformation curves were measured by the viscosity curve (Viscosity of low-viscosity liquids mode). The zero-shear viscosity is the viscosity measured at a shear rate of 0.00251  $\text{s}^{-1}$ . Oscillatory measurements were performed with Amplitude sweep (yield and flow stress study) with an angular frequency of 1  $\text{s}^{-1}$ . The composite film's internal properties were examined by using X-ray diffraction (XRD, Rigaku D/Max-2200/PC X-ray Diffractometer), Scanning electron microscopy (SEM, TESCAN/Vega 2 LSU), transmission electron microscopy (TEM, Tecnai G2 F30 S-Twin, FEI) and energy-dispersive X-ray spectroscopy (EDAX, Bruker/Quantax 200). Thermal properties of the composite films were performed by using thermogravimetric analyzer (TGA, TA instruments, Discovery TGA 5500) with a ramp-up rate of 5 °C–800 °C under  $\text{N}_2$  atmosphere. The films were cut into 1 cm × 3 cm. At room temperature, the tensile properties of the composite films were tested on using a universal testing machine (UTM, ST-1000, SALT, Korea) with a strain rate of 10 mm/min. Electrical conductivity were tested by resistivity meter (RSD-40K, S. DSA). Flexibility were tested by radius bending tester (JIBT-610, JINIL TECH). EMI SE was measured based on the waveguide method with a vector network analyzer (KEYSIGHT, PNA Network analyzer, N5222B) in the frequency range of 8.2–12.4 GHz (X-band) and 26.5–40 GHz (Ka-band). The power coefficients of reflection (R), absorption (A), transmission (T), and the total EMI shielding efficiency (EMI SE<sub>T</sub>) are calculated from the scattering parameters ( $S_{11}$  and  $S_{21}$ ) according to the following equations.

$$R = |S_{11}|^2 = |S_{22}|^2$$

$$T = |S_{21}|^2 = |S_{12}|^2$$

$$A = 1 - R - T$$

$$SE_R = -10 \log(1 - R)$$

$$SE_A = -10 \log\left(\frac{T}{1 - R}\right)$$

$$SE_T = SE_A + SE_R$$

### 3. Results and discussion

#### 3.1. Synthesis, functionalization, and characterization of $\text{Ti}_3\text{C}_2\text{T}_x$ MXene-Based composites

To establish the properties of the materials used, we first characterized the  $\text{Ti}_3\text{C}_2\text{T}_x$  MXene and the water-borne polyimide (W-PI).  $\text{Ti}_3\text{C}_2\text{T}_x$  MXene was synthesized from the  $\text{Ti}_3\text{AlC}_2$  MAX phase by the MILD etching method [26], with details in the experimental section. SEM image in Fig. S1A shows that the typical lateral size of the MXene sheets was approximately 4  $\mu\text{m}$ . Also, it was observed that MXene was well delaminated into single sheets, indicated by their high

transparency. The chemical structure of  $\text{Ti}_3\text{C}_2\text{T}_x$  was analyzed using X-ray photoelectron spectroscopy (XPS). The Ti 2p peak was fitted with four doublets in Ti 2p<sub>1/2</sub> and Ti 2p<sub>3/2</sub> with an area ratio of 1:2 where each doublet peak is separated by 5.8 eV. The Ti 2p<sub>3/2</sub> peaks centered at 454.8, 455.7, 456.9, and 458.7 eV were assigned to Ti–C, Ti<sup>2+</sup>, Ti<sup>3+</sup>, and TiO<sub>2</sub>, respectively. The low intensity of the TiO<sub>2</sub> peak in the Ti 2p peak indicates that the MXene is high quality with minimal oxidation. The O 1s peak and F 1s peak also were obtained to analyze the functional groups of  $\text{Ti}_3\text{C}_2\text{T}_x$ . The O 1s peak was divided into four major peaks centered at 529.4, 529.9, 531.9, and 533.8 eV, corresponding to TiO<sub>2</sub>, Ti–O–Ti, Ti–OH, and Ti–H<sub>2</sub>O, respectively. The Ti–O–Ti and Ti–OH peak suggest that –O and –OH functional groups are present on the surface of the  $\text{Ti}_3\text{C}_2\text{T}_x$ . Also, The Ti–F<sub>x</sub> peak in the F 1s peak region indicates the simultaneous presence of –F functional groups on the surface. Additionally, the synthesis and characterization of W-PAAS are shown in Fig. S2. The synthetic process for BPDA/pPDA-based W-PAAS is depicted in Fig. S2A. In this process, 3,3',4,4'-Biphenyltetracarboxylic dianhydride (BPDA) and *p*-phenylenediamine (pPDA) were first carefully dried in a vacuum oven at 200 °C and 70 °C for 6 h, respectively, to remove any residual moisture, ensuring optimal reactivity during the polymerization. Subsequently, the tertiary amine, 1,2-dimethylimidazole (DMIZ), was added to facilitate the polycondensation reaction between BPDA and pPDA, which occurred in an aqueous medium [25]. The reaction was monitored for complete synthesis under controlled conditions, leading to the formation of the polyimide-based W-PAAS. The successful synthesis was confirmed through several analytical techniques, including <sup>1</sup>H NMR spectroscopy (Fig. S2B), size exclusion chromatography (SEC, Fig. S2C), and ATR-IR spectroscopy (Figs S2D and S2E). These analyses validate the thermal imidization process and the structural transformation from W-PAAS to W-PI, which constitutes the foundational matrix for the polyimide used in this study.

Pristine  $\text{Ti}_3\text{C}_2\text{T}_x$  MXene, despite its outstanding properties, encounters significant dispersion challenges in aqueous W-PAAS systems, as illustrated in Fig. 1A [20]. This is due to the aggregation between negatively charged MXene sheets and the positively charged W-PAAS, which detrimentally affects their uniform hybridization in composite systems. To address this limitation, PCE was employed as a functionalizing agent, as shown in Fig. 1B [27]. PCE functionalization enhances the solubility and dispersion of MXene sheets, facilitating their uniform integration into the polymer matrix. As highlighted in Fig. 1C, the PCE-MXene is expected to create a uniform dispersion with W-PAAS without having the charge-induced aggregation issues that are observed for pristine MXene systems.

The rheological properties of PCE-MXene in W-PAAS solutions (PMS) were analyzed to optimize the composite formulation for enhanced processability and performance. To verify the absence of aggregation, Fig. S3 presents real images of PMS-30, PMS-50, PMS-70, and PMS-90, corresponding to MXene-to-PI mass ratios of 3:7, 5:5, 7:3, and 9:1, respectively. These images confirm uniform distribution across all compositions, ensuring the structural integrity and functionality of the composites. Fig. S4 provides supporting evidence, with Fig. S4A showing viscosity measurements and Fig. S4B illustrating overall rheological behavior. Regardless of solid content ratio variations, all dispersions exhibit typical viscoelastic properties, commonly observed in well-dispersed 2D material suspensions. The high viscosity at low shear rates and low viscosity at high shear rates make these formulations well-suited for large-scale film and coating applications. Fig. 1D shows that at a fixed shear rate of 20  $\text{s}^{-1}$ , PMS-70 exhibits the highest viscosity, suggesting that MXene-PCE interactions influence the internal solid structure. Beyond viscoelastic properties, the high zero-shear viscosity enhances the long-term stability of composite dispersions, making them effective for industrial applications. To further support the interaction mechanism between W-PAAS and PCE, we performed density functional theory (DFT) calculations and analyzed the electron density difference of each molecule. As shown in Fig. S5, W-PAAS exhibits an overall positive electrostatic potential, while PCE displays strong electron



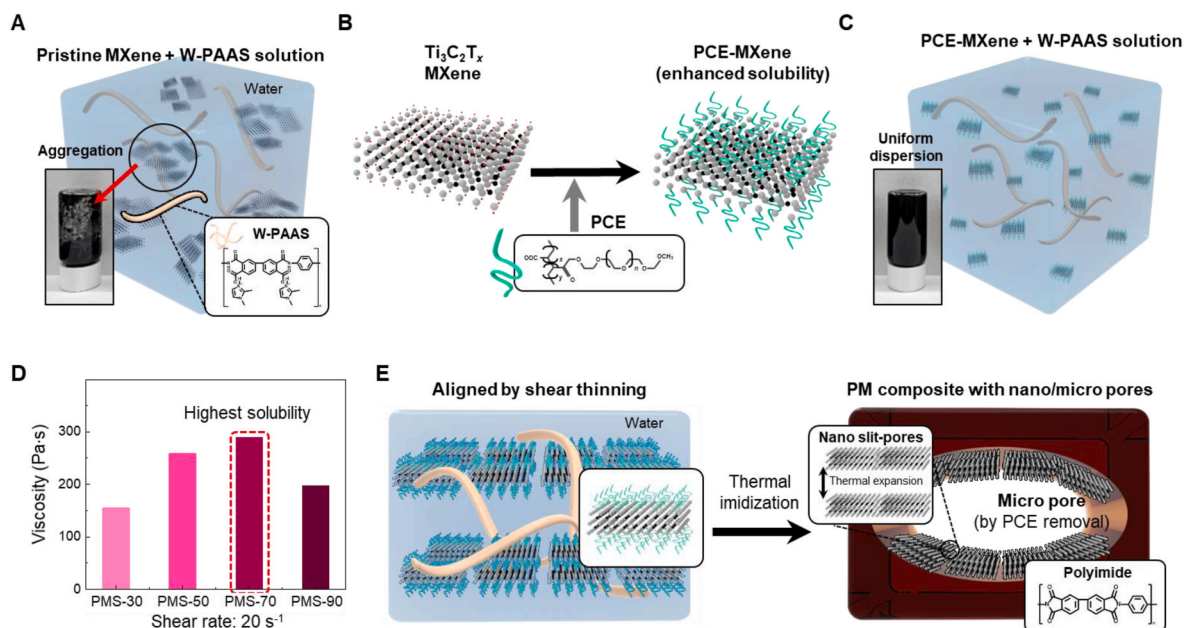


**Fig. 1. Characterization and properties of pristine and PCE-functionalized MXene in W-PAAS solutions.** (A) Schematic illustration of pristine  $\text{Ti}_3\text{C}_2\text{T}_x$  MXene highlighting its aggregation behavior in aqueous solutions. The inset shows a real image of aggregated MXene sheets. (B) Schematic of the polycarboxylate ether (PCE) functionalization process, demonstrating the improved solubility and dispersion of MXene in W-PAAS solutions. (C) Schematic representation of the high solubility and uniform dispersion of PCE-functionalized MXene (PCE-MXene) in W-PAAS solutions. The inset displays a real image of the homogeneous dispersion achieved with PCE treatment. (D) Viscosity of PMS with varying MXene-to-polyimide ratios, measured at a fixed shear rate of  $20 \text{ s}^{-1}$ , showing the highest viscosity at a 3:7 ratio (PMS-70). (E) Schematic of the dual pore formation mechanism during thermal imidization. Micro-pores form due to PCE evaporation, while nano-pores emerge from the thermal expansion of MXene, significantly enhancing EMI shielding performance.

accumulation around oxygen atoms. This charge separation suggests a favorable electrostatic interaction between the two components, which likely contributes to the stable dispersion of PCE-functionalized MXene in the W-PAAS matrix.

Fig. 1E illustrates the structural transformations upon thermal imidization of W-PAAS into W-PI in the presence of PCE-MXene. During this process, PMS was assembled into a film using a slot-die coater, in which shear thinning facilitates the laminar alignment of PCE-MXene nanosheets. After film formation, heat was sequentially applied to the film which leads to three main structural transformations. First, W-PAAS was transformed into PI through thermal imidization. Second, PCE is degraded at high temperatures, in which the evolution of gaseous hydrocarbon species and water during the removal of PCE creates micro-pores within the structure. Third, the interlayer spacing between adjacent MXene sheets is increased due to the removal of intercalated species within the confined composite structure. The evolution of such pores is expected to play a significant role in enhancing the EMI shielding performance by providing multiple pathways for the reflection and absorption of electromagnetic waves, thereby improving the composite's overall effectiveness.

### 3.2. Pore formation mechanisms in PM composites

The PCE- $\text{Ti}_3\text{C}_2\text{T}_x$  MXene/PI (PM-XX) composite films were fabricated through a sequential process consisting of mixing, solution casting, and thermal imidization. In the designation PM-XX, "XX" represents the weight fraction of MXene in the composite. The PM-XX composites were systematically analyzed to assess their morphological, electrical, and structural properties. Scanning electron microscopy (SEM) images in Fig. 2A illustrate the morphology of PM composites with different MXene contents (PM-30, PM-50, PM-70, and PM-90). These images demonstrate that the shear thinning effect during film formation effectively aligned the MXene sheets, resulting in a well-ordered, layered structure. Additionally, SEM-EDX elemental mapping (Fig. S6) further confirms the uniform distribution of MXene, supporting the formation of

efficient conductive networks even in highly porous samples such as PM-70. Fig. 2B compares the electrical and mechanical properties of the PM composites across different MXene-to-polyimide ratios. Electrical conductivity exhibits a linear increase with higher MXene content, ranging from 90.2 to 1111 S/cm across PM-30 to PM-90, attributed to the enhanced conductive network formed by the aligned MXene sheets. Interestingly, while tensile strength typically declines with increasing MXene concentration, it remains stable between PM-50 and PM-70. This stability highlights the importance of uniform dispersion in preserving mechanical integrity, even at elevated MXene concentration. Consequently, the PM-70 composite emerges as the optimal formulation, balancing high electrical conductivity with robust mechanical properties, making it well-suited for advanced applications. Fig. S5 supports these findings by presenting stress-strain curves for all PM composites, illustrating their mechanical behavior across compositions.

The pore generation behavior during the synthesis of PM composites was investigated through thermogravimetric analysis (TGA), where Fig. 2C depicts the change in weight prior to imidization. The TGA results show that the decomposition of the PCE-MXene mixture begins near  $250^\circ\text{C}$ , which overlaps with the imidization range of W-PAAS. Given that thermal imidization reaches completion above  $350^\circ\text{C}$ , as confirmed by additional TGA data (Fig. S9), PCE is expected to fully decompose during the curing process, enabling in situ pore formation. When the temperature is gradually increased during thermal treatment, the TGA analysis reveals two distinct weight loss events. Initially, at around  $100^\circ\text{C}$ , a slight decrease in weight occurs, corresponding to the loss of water and DMIZ as the imidization begins. As the temperature rises further, around  $350^\circ\text{C}$ , a significant weight loss is observed, which corresponds to the evaporation of the PCE treatment from the MXene. This dual process—both imidization and PCE evaporation—results in the formation of a porous structure in the final composite material. The removal of PCE from the MXene surface during thermal treatment creates voids and contributes to the overall porosity of the composite, while the imidization reaction solidifies the polyimide matrix, reinforcing the structure. The final composite films exhibit a unique porous

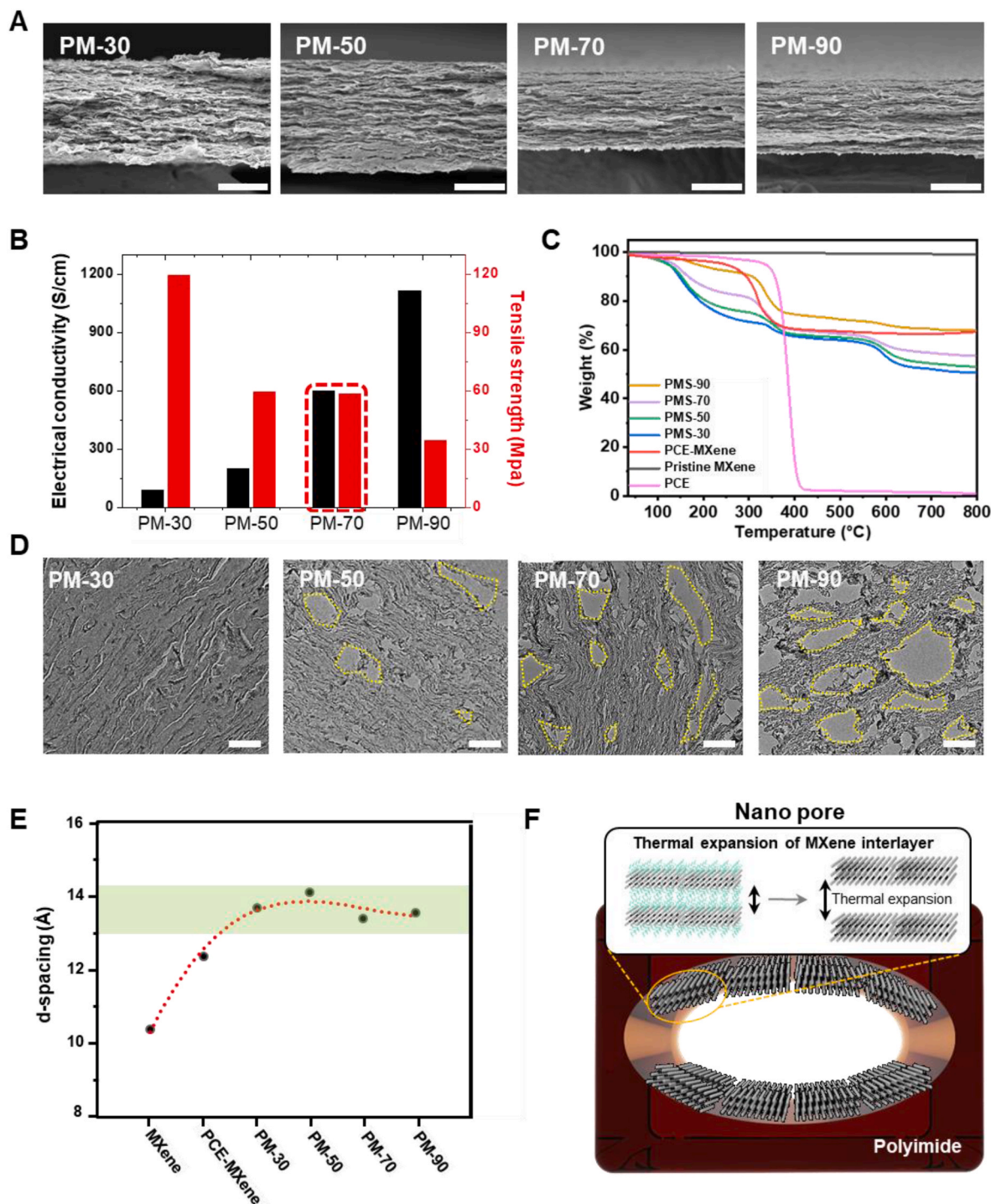


**Fig. 2. Morphological, electrical, and structural properties of PM composites.** (A) Scanning electron microscopy (SEM) images of PM composites with varying MXene-to-polyimide ratios (PM-30, PM-50, PM-70, and PM-90), showing well-aligned and layered structures formed during the shear thinning process. (Scale bar = 2  $\mu$ m). (B) Comparison of electrical conductivity and tensile strength of PM composites as a function of MXene content. (C) Thermogravimetric analysis (TGA) results of PM composites, showing complete removal of PCE during imidization, which leads to micro-pore formation. (D) Transmission electron microscopy (TEM) images of PM composites, revealing an increase in micro-pore formation with higher MXene content due to greater PCE presence. All scales are 2  $\mu$ m. (E) The interlayer d-spacing of MXene sheets after thermal imidization was analyzed using X-ray diffraction, revealing the formation of nano-pores within the composite structure. (F) Schematic illustration of hierarchical dual pore formation mechanism. Micro-pores are generated through PCE evaporation, while nano-pores are created by the thermal expansion of MXene sheets.

morphology, which can be understood through the combined effects of the thermal imidization process and the simultaneous loss of PCE from the MXene. Additional TGA data for W-PAAS, W-PI, and PM composites are presented in Fig. S6, which clearly demonstrate the water loss during W-PAAS imidization and the thermal decomposition of composites after

imidization. It could be intuitively seen that composites with lower MXene content show larger weight loss due to the decomposition of PI near 600 °C, while the MXene layer is known to be stable up to 800 °C.

Transmission electron microscopy (TEM) images in Fig. 2D directly show the formation of pores, showing that the number of micro-pores

increases with MXene concentration. This phenomenon is attributed to the higher PCE content in composites with elevated MXene proportions. The porous nature of the composites was further quantified using Brunauer-Emmett-Teller (BET) analysis, as presented in Fig. S7, which demonstrates a significant increase in internal surface area from PM-30 to PM-90, highlighting the impact of pore formation on the composite structure. Notably, BET results show that pore structures are not detected for films that have been only heated up to 250 °C, which is below the PCE decomposition temperature, as shown in Fig. S8. Consistent with the dual pore-forming mechanism, BET analysis (Fig. S12) revealed an increasing volume of nanopores (5–50 nm) with

higher MXene and PCE content, supporting the enhanced EMI shielding performance of PM-70 and PM-90. These results support the hypothesis that PCE evaporation during imidization plays a crucial role in micro-pore formation. This structural transformation is further corroborated by the X-ray diffraction (XRD) patterns of PM composites (Fig. S9) and the corresponding  $d$ -spacing data in Fig. 2E. To further investigate the structural evolution during thermal imidization, XRD measurements were conducted on samples treated at 100 °C, 280 °C, and 380 °C. As shown in Fig. S14, the (002) diffraction peak of MXene progressively shifted to lower angles with increasing temperature, indicating an expansion of the interlayer spacing. This  $d$ -spacing increase is likely due

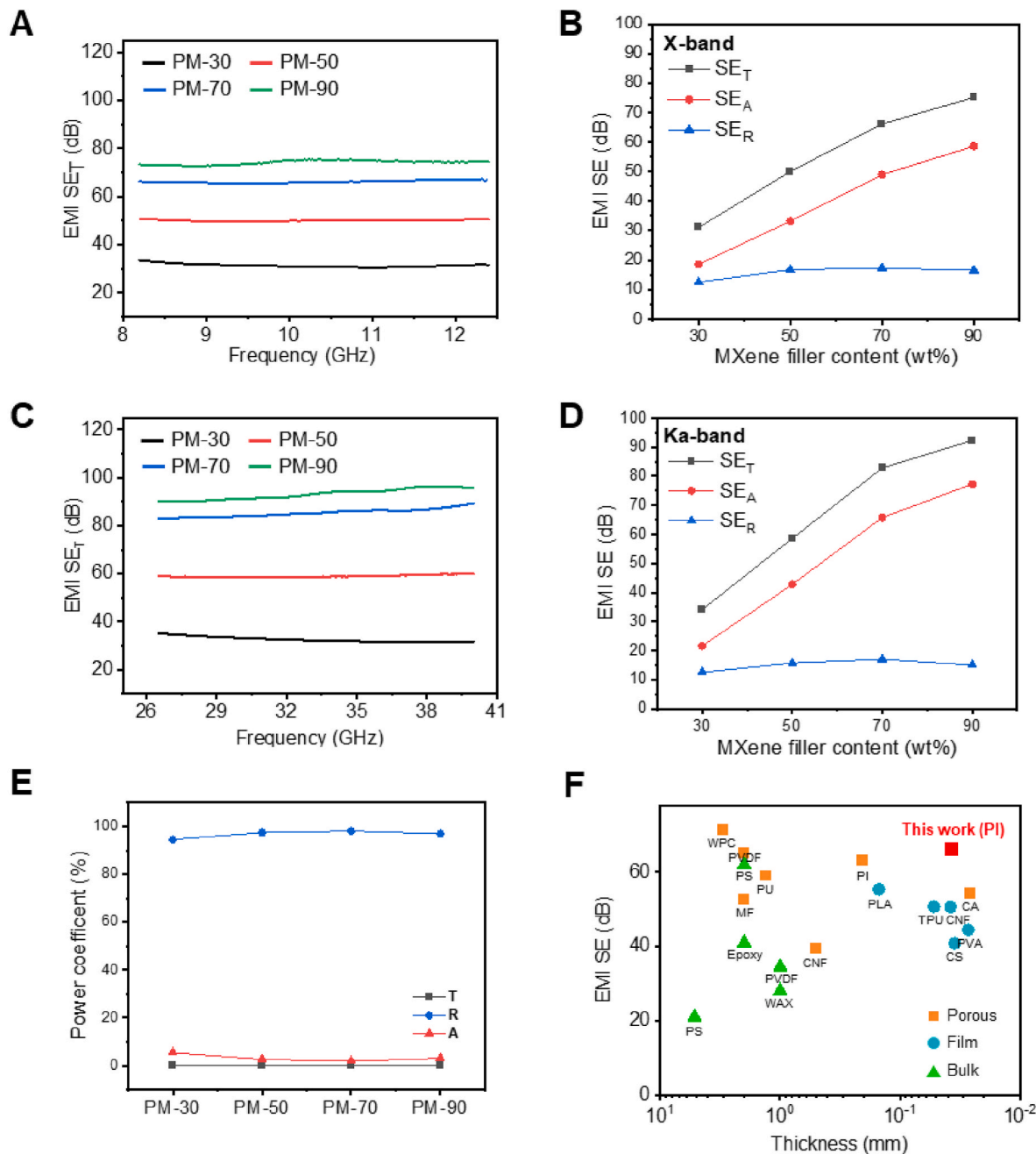


**Fig. 3.** EMI shielding performance of PM composites in X-band and Ka-band ranges. (A) EMI shielding effectiveness (EMI SE) of PM composites (PM-30, PM-50, PM-70, and PM-90) in the X-band. (B) Comparison of EMI SE<sub>T</sub>, SE<sub>A</sub>, and SE<sub>R</sub> values across PM composites in the X-band. (C) EMI SE performance in the Ka-band, with similar trends to the X-band but exhibiting higher SE<sub>T</sub> values. (D) Comparison of SE<sub>T</sub>, SE<sub>A</sub>, and SE<sub>R</sub> values across PM composites in Ka-band, showing a consistent increase with higher MXene content, while SE<sub>R</sub> shows minimal variation. (E) Power coefficients for reflection (R), absorption (A), and transmission (T) of PM composites, illustrating the reflection-dominant shielding mechanism. (F) Comparative analysis of EMI SE and thickness of PM-70 with other MXene/polymer and 2D material-based composites, demonstrating PM-70's superior performance with an EMI SE of 66.1 dB and a thickness of 0.037 mm.



to internal gas release and thermal expansion associated with PCE decomposition, supporting the development of hierarchical porosity. During composite formation, the presence of PCE initially increases the interlayer spacing of MXene sheets. Following PCE removal, instead of reverting to the original spacing, the d-spacing expands further due to the thermal expansion of MXene sheets during the imidization process. This irreversible expansion indicates the formation of nano-pores within the composite structure. Fig. 2F schematically depicts the dual pore formation mechanism: micro-pores are generated through PCE evaporation, while nano-pores result from the thermal expansion of MXene sheets.

### 3.3. EMI shielding performance of PM composites

To evaluate the EMI shielding performance of the PM composites, we analyzed their shielding effectiveness (EMI SE) across two critical frequency bands: the X-band (8.2–12.4 GHz), widely used in radar communication, and the Ka-band (26.5–40 GHz), a major band for 5G communication. The results, presented in Fig. 3, provide comprehensive insights into the shielding mechanisms and their dependence on MXene content. In the X-band range, as detailed in Fig. 3A, the total shielding effectiveness ( $SE_T$ ) values for PM-30, PM-50, PM-70, and PM-90 were measured as 31.4, 50.1, 66.1, and 74.2 dB, respectively, indicating a clear and consistent increase in shielding performance with higher MXene content. Notably, the  $SE_T$  values remained stable across the frequency band, demonstrating the reliability of the composites. By decomposing  $SE_T$  into reflection ( $SE_R$ ) and absorption ( $SE_A$ ) components, Fig. 3B and the supporting data in Fig. S10 reveal that  $SE_A$  values significantly increased with MXene content, ranging from 19.0 dB for PM-30 to 57.6 dB for PM-90, while  $SE_R$  values remained relatively constant at approximately 10–20 dB. As the MXene content increased, the shielding effectiveness due to absorption ( $SE_A$ ) accounted for a larger proportion of the total EMI shielding, while the contribution from reflection ( $SE_R$ ) remained nearly constant. A similar trend was observed in the Ka-band, as shown in Fig. 3C. The total shielding effectiveness ( $SE_T$ ) values for PM-30, PM-50, PM-70, and PM-90 were 32.7, 58.9, 85.0, and 93.1 dB, respectively, demonstrating a clear correlation between increased MXene content and enhanced shielding performance (Fig. 3D). The overall shielding performance is better at higher frequencies, as electromagnetic waves interact more frequently with the shielding material at the molecule or atom level, leading to better energy absorption. Also, as the skin depth becomes smaller at higher frequencies, the effective thickness is increased to eventually enhance the shielding effectiveness.

The exceptional performance of the PM composites can be attributed to the synergistic effects of high electrical conductivity, uniform dispersion of MXene sheets, and the development of internal porous structures. The inherent conductivity of MXene ensures that a substantial portion of incident electromagnetic waves is reflected at the composite's surface, as evidenced by  $SE_R$  values in the range of 10–20 dB, corresponding to over 90 % reflectivity. As shown in Fig. 3E, the power coefficients for reflectivity, absorptivity, and transmissivity confirm a reflection-dominant shielding mechanism. On the other hand, the internal structure of the composites plays an equally crucial role in attenuating the remaining waves, evidenced by the high  $SE_A$  values. The  $SE_A$  value can be first estimated using the Simon formalism. In the case where the shielding material has sufficient electrical conductivity without magnetism, the equation for absorption contributions can be expressed as follows:

$$SE_A \text{ (dB)} = 1.7t\sqrt{\sigma f}$$

where  $\sigma$  (S/cm),  $t$  (cm), and  $f$  (MHz) refer to sample electrical conductivity, sample thickness, and EM wave frequency, respectively. Taking PM-70 as an example, the calculated  $SE_A$  values at the X-band and K-band are 17.0 and 26.0 dB, respectively. In both cases, the calculated

values are lower than the measured  $SE_A$  values at the X-band and Ka-band, which are 48.6 and 65.8 dB, respectively. This is because the PM composites have extensive porous structures that can have addition effects, which are not taken into consideration in the equation above. The hierarchical porous structures, formed through PCE evaporation during imidization and the thermal expansion of MXene sheets, enable internal reflections and scattering events, effectively attenuating electromagnetic waves that penetrate the surface. As the MXene content increases, a larger number of pores evolve in the composites, enhancing their contribution to the total shielding effectiveness through increased  $SE_A$  values. Consequently, the PM-90 composite, which has the highest MXene content, naturally exhibits the greatest EMI shielding efficiency. However, PM-70 was identified as the optimal material due to its balanced performance and mechanical durability, making it more suitable for practical applications. Although PM-90 shows the highest electrical conductivity and shielding effectiveness, its tensile strength drops to 35 MPa, indicating poor mechanical integrity. In contrast, PM-70 offers a better balance between electrical and mechanical properties (tensile strength = 59 MPa). Similar trade-offs have been observed in other high-loading MXene/polymer systems, where mechanical performance deteriorates beyond a certain filler threshold due to disrupted polymer chain alignment [28].

Finally, Fig. 3F compares the performance of PM composites with other MXene- and 2D material-based polymer composites, highlighting the superior EMI shielding efficiency of the PM-70 composite [29–45]. With an EMI SE of 66.1 dB at an ultrathin thickness of 0.037 mm, PM-70 outperforms existing materials in both shielding effectiveness and compactness, highlighting its potential for lightweight, high-performance EMI shielding applications in modern electronic devices. This comprehensive analysis describes the critical role of MXene content and the evolution of internal porous structures in achieving exceptional EMI shielding performance. These results provide a pathway for developing advanced composite materials tailored to the requirements of next-generation communication and electronic systems.

### 3.4. Scalability, flexibility, and stability of PM composite films

To evaluate the scalability, flexibility, and stability of the PM composite films, a series of experiments was conducted, as illustrated in Fig. 4. Fig. 4A presents a photograph of a PM-XX composite film fabricated using a slot-die coating process, where the PMS-XX solution was dispensed onto a PET substrate at a flow rate of 2 mL/min, with the coating head moving at 40 mm/s. Following coating, the film was carefully separated from the substrate and thermally imidized through sequential steps up to 380 °C, yielding free-standing PM composite films measuring 3 cm × 3 cm. Fig. S11 highlights the scalability of the slot-die coating process through photographs of large-area coated films, demonstrating its potential for industrial-scale applications. This scalability is clearly demonstrated in Movie S1, which documents the continuous slot-die coating process, and Movie S2, which captures the bending test procedure, effectively showcasing the flexibility and durability of the PM composite films. Fig. 4B displays a large-area PM composite film (15 cm × 15 cm) fabricated via slot-die coating, demonstrating the scalability of the method. This continuous coating process ensures uniform film quality over a large area, making it suitable for industrial-scale production. To evaluate the thickness uniformity of the large-area PM-70 film, we measured film thickness at 25 locations (5 × 5 grid) across a 15 × 15 cm<sup>2</sup> sample. The variation was minimal, confirming the feasibility of uniform film fabrication over large areas (Fig. S17). The flexibility of the PM composite films was assessed through bending tests, as shown in Fig. 4C. The cyclic bending test was conducted at a frequency of 1 cycle per second, with a 0.5 s rest between each cycle. Samples measuring 1 cm × 3 cm were tested for their minimum bending radii using a bending test machine, which revealed bending radii of 1.75 mm, 1.5 mm, 1.5 mm, and 1.2 mm for PM-30, PM-50, PM-70, and PM-90, respectively. These results highlight the high

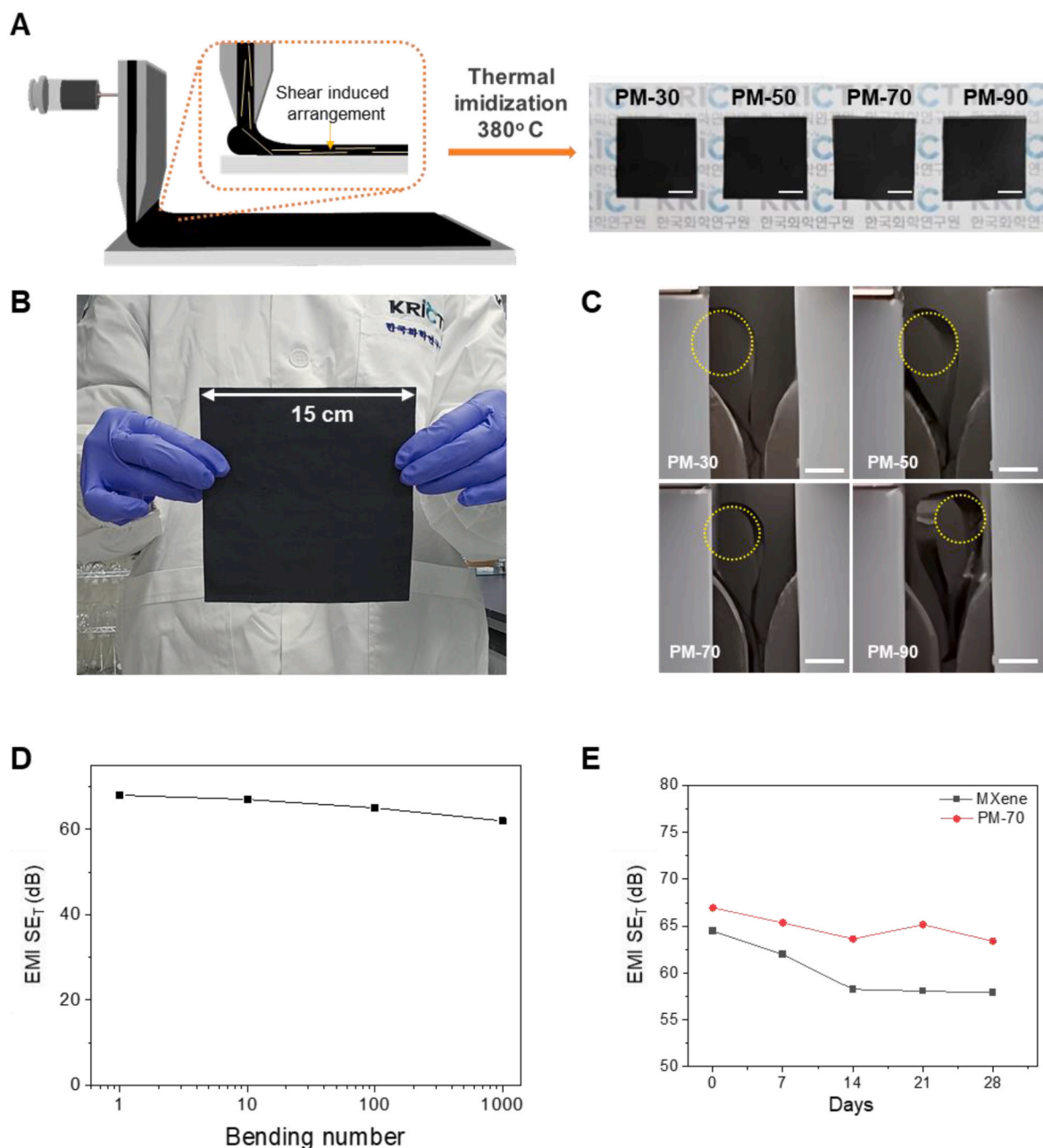


**Fig. 4. Large-area fabrication, flexibility, and stability of PM composite films.** (A) Photograph of PM composite films fabricated via slot-die coating onto a PET substrate and thermally imidized, showing a film size of 3 cm × 3 cm. (B) Large-area PM composite film (15 cm × 15 cm) produced using the slot-die coating method, demonstrating scalability. (C) Bending test of PM composite films with a sample size of 1 cm × 3 cm. Bending radii of PM-30, PM-50, PM-70, and PM-90 are 1.75 mm, 1.5 mm, 1.5 mm, and 1.2 mm, respectively. (D) EMI SE retention after 1000 bending cycles, with PM composites maintaining over 95 % of their initial performance. (E) Long-term stability of PM-70 compared to pristine MXene. After one month at room temperature, PM-70 retains high EMI SE due to polyimide protection, while MXene exhibits significant degradation. (F) Summary of stability and flexibility tests, emphasizing the potential of PM composites for durable, flexible and adaptable EMI shielding applications.

flexibility of all compositions, with all films exhibiting bending radii of less than 2 mm, emphasizing the robustness and adaptability of the PM composites for flexible electronic applications.

To further assess mechanical durability, Fig. 4D presents the EMI shielding performance of PM composite films after 1000 bending cycles. Remarkably, the shielding effectiveness retained over 95 % of its initial value, even under repeated bending, demonstrating the exceptional mechanical resilience of the films. Additionally, Fig. S12 shows that the electrical conductivity of the PM composites also maintained over 95 % of its initial value after 1000 bending cycles, further confirming their structural integrity and functional durability. The long-term stability of

the PM composites was assessed under ambient conditions, as shown in Fig. 4E, which compares the EMI shielding performance of pristine MXene and PM-70 composite films after one month of storage at room temperature. While the shielding performance of pristine MXene significantly declined due to oxidation, the PM-70 composite largely retained its initial performance. This stability is attributed to the protective PI matrix, which effectively prevents environmental degradation of the MXene sheets, ensuring prolonged functionality. These results collectively demonstrate the scalability, flexibility, mechanical durability, and long-term stability of PM composite films, establishing them as promising candidates for practical applications in flexible and durable



EMI shielding materials.

#### 4. Conclusion

This study demonstrates the successful development of high-performance PM composites through a scalable slot-die coating process. The use of polycarboxylate ether (PCE) as a functionalizing agent significantly enhanced the solubility, dispersion, and alignment of  $\text{Ti}_3\text{C}_2\text{T}_x$  MXene sheets within a water-borne polyimide (W-PI) matrix. The unique hierarchical porous structures, created via PCE evaporation and the thermal expansion of MXene during imidization, significantly enhanced internal reflection and absorption pathways, establishing  $\text{SE}_A$  as the dominant shielding mechanism. The resulting composites exhibited outstanding electrical conductivity, mechanical robustness, and superior EMI shielding performance, with the PM-70 composite achieving an EMI SE of 66.1 dB in the X-band and 85.0 dB in the Ka-band at an ultrathin thickness of 0.037 mm. These films demonstrated remarkable flexibility, achieving bending radii below 2 mm for all compositions, and maintained over 95 % of their initial shielding and electrical properties after 1000 bending cycles. Furthermore, the polyimide matrix effectively protected the MXene sheets from oxidation, ensuring long-term environmental stability. The integration of scalability, flexibility, and durability in the PM composites makes them highly suitable for modern electronic applications where compact, lightweight, and reliable EMI shielding materials are essential. This work suggests the potential of  $\text{Ti}_3\text{C}_2\text{T}_x$  MXene-based composites as a versatile platform for advancing EMI shielding technologies, meeting the demands of next-generation communication and electronic systems.

#### CRediT authorship contribution statement

**Na Gyung Kim:** Writing – original draft, Methodology, Investigation, Formal analysis, Data curation. **Jeong Min Jang:** Writing – original draft, Methodology, Investigation, Formal analysis, Data curation. **Young-Jun Kim:** Writing – original draft, Methodology, Investigation, Formal analysis. **Ju Yeon Kim:** Methodology, Formal analysis. **Dong-hyeon Kang:** Investigation, Methodology. **Jongmin Park:** Validation, Investigation, Formal analysis. **Jong Chan Won:** Validation, Methodology, Investigation. **Sang-Woo Kim:** Investigation, Methodology. **Dae Woo Kim:** Writing – review & editing, Supervision, Formal analysis, Conceptualization. **Seon Joon Kim:** Writing – review & editing, Funding acquisition, Formal analysis, Conceptualization. **Yun Ho Kim:** Writing – review & editing, Writing – original draft, Supervision, Funding acquisition, Conceptualization.

#### Declaration of generative AI and AI-assisted technologies in the writing process

During the preparation of this work the author(s) used [OpenAI/ChatGPT-4o] in order to [English Correction]. After using this tool/service, the author(s) reviewed and edited the content as needed and take(s) full responsibility for the content of the publication.

#### Declaration of competing interest

The authors declare that they have no known competing financial interests or personal relationships that could have appeared to influence the work reported in this paper.

#### Acknowledgment

N.G.K, J.M.J., Y.-J.K. contributed equally to this work. This work was supported by KRICT core project (KS2521-20), the National Research Foundation of Korea (NRF) grant funded by the Ministry of Science, ICT, and Future Planning, Korea (NRF-2021R1A2C2006771). This research was also supported by the National Research Council of Science &

Technology (NST) grant by the Korea government (MSIT) (CRC22031-000) and by the Ministry of Trade, Industry, and Energy (MOTIE), Korea, under the “Global Industrial Technology Cooperation Center program” (Grant: P0028332) supervised by the Korea Institute for Advancement of Technology (KIAT), Korea.

#### Appendix. ASupplementary data

Supplementary data to this article can be found online at <https://doi.org/10.1016/j.compositesb.2025.112805>.

#### Data availability

Data will be made available on request.

#### References

- [1] Kuang X, Chen K, Dong W, Zhang Y, Lin C, Yu Z. Lightweight and flexible MXene/polymer composite films with outstanding electromagnetic interference shielding performance. *Adv Mater* 2021;33:2101866. <https://doi.org/10.1002/adma.202101866>.
- [2] Song W, Zhang Y, Li D, Cheng H, Wang Z. Self-powered flexible electronic skin for real-time health monitoring. *ACS Nano* 2020;14:15416–26. <https://doi.org/10.1021/acsnano.0c05908>.
- [3] Zhu P, Zhang Y, Cao Y, Wang C. Advanced materials for energy storage devices: state of the art and perspectives. *Chem Rev* 2022;122:14834–85. <https://doi.org/10.1021/acs.chemrev.2c00321>.
- [4] Ma M, Liang X, Tao W, Peng Q, Shao W, Chen S, Shi Y, He H, Zhu Y, Wang X. Waterborne polyurethane aerogel with asymmetric gradient structure formed by density-induced self-stratification for absorption-dominated electromagnetic interference shielding. *Compos Struct* 2024;342:118259. <https://doi.org/10.1016/j.comstruct.2024.118259>.
- [5] Peng Q, Ma M, Chu Q, Lin H, Tao W, Shao W, Chen S, Shi Y, He H, Wang X. Absorption-dominated electromagnetic interference shielding composite foam based on porous and bi-conductive network structures. *J Mater Chem A* 2023;11:10857–66. <https://doi.org/10.1039/D3TA01369C>.
- [6] Shao W, Zhang X, Liang X, Tao W, Ma M, Chen S, Shi Y, He H, Zhu Y, Wang X. Cellulose nanofiber-based nanocomposite films with efficient electromagnetic interference shielding and fire-resistant performance. *ACS Appl Mater Interfaces* 2024;16:32. <https://doi.org/10.1021/acsami.4c10660>.
- [7] Liang C, Gu Z, Zhang Y, Ma Z, Qiu H, Gu J. Multifunctional MXene/polyimide films with outstanding thermal conductivity and electromagnetic interference shielding. *Nano-Micro Lett* 2021;13:181. <https://doi.org/10.1007/s40820-021-00681-9>.
- [8] Yao Y, Jin S, Zou H, Li L, Ma X, Lv G, Gao F, Lv X, Shu Q. High-performance MXene composite films with superior mechanical and EMI shielding properties. *J Mater Sci* 2021;56:6549–80. <https://doi.org/10.1007/s10853-020-05599-7>.
- [9] Wang Y, Peng H-K, Li T-T, Shiu B-C, Zhang X, Lou C-W, Lin J-H. Multi-scale structured fabrics for effective electromagnetic interference shielding. *J Mater Sci* 2020;55:13008–22. <https://doi.org/10.1007/s10853-020-04881-x>.
- [10] Wang Y, Zhao W, Tan L, Li Y, Qin L, Li S. Novel biodegradable conductive composites for smart wearable sensors. *Molecules* 2023;28:5628. <https://doi.org/10.3390/molecules28145628>.
- [11] Barani Z, Kargar F, Ghafouri Y, Ghosh S, Godziszewski K, Seyedmahmoudbaraghani S, Yashchishyn Y, Cywiński G, Remyantsev S, Salguero TT, Balandin AA. Thermal and electrical transport in 2D materials: a review. *Adv Funct Mater* 2021;31:2100829. <https://doi.org/10.1002/adfm.202100829>.
- [12] Zhan X, Si C, Zhou J, Sun Z. Electronic and thermal transport in boron-based 2D materials. *Nanoscale Horiz* 2020;5:235–58. <https://doi.org/10.1039/C9NH00530J>.
- [13] Zhang W, Ji X-X, Ma M-G. High-strength nanocellulose aerogels reinforced by boron nitride nanosheets. *Chem Eng J* 2023;458:141402. <https://doi.org/10.1016/j.cej.2023.141402>.
- [14] Zhang CJ, Pinilla S, McEvoy N, Cullen CP, Anasori B, Long E, Park S-H, Seral-Ascaso A, Shmeliov A, Krishnan D, Morant C, Liu X, Duesberg GS, Gogotsi Y, Nicolosi V. Oxidation stability of colloidal two-dimensional titanium carbides (MXenes). *Chem Mater* 2017;29:4848–56. <https://doi.org/10.1021/acs.chemmater.7b00745>.
- [15] Ghidui M, Lukatskaya MR, Zhao M-Q, Gogotsi Y, Barsoum MW. Conductive two-dimensional titanium carbide ‘clay’ with high volumetric capacitance. *Nature* 2014;516:78–81. <https://doi.org/10.1038/nature13970>.
- [16] Naguib M, Kurtoglu M, Presser V, Lu J, Niu J, Heon M, Hultman L, Gogotsi Y, Barsoum MW. Two-dimensional nanocrystals produced by exfoliation of  $\text{Ti}_3\text{AlC}_2$ . *Adv Mater* 2011;23:4248–53. <https://doi.org/10.1002/adma.201102306>.
- [17] Gong K, Zhou K, Qian X, Shi C, Yu B. MXene as emerging nanofillers for high-performance polymer composites: a review. *Compos B Eng* 2021;217:108867. <https://doi.org/10.1016/j.compositesb.2021.108867>.
- [18] Amin I, van den Brekel H, Nemani K, Batyrev E, de Vooy A, van der Weijde H, Anasori B, Shiju NR.  $\text{Ti}_3\text{C}_2\text{T}_x$  MXene polymer composites for anticorrosion: an overview and perspective. *ACS Appl Mater Interfaces* 2022;14:42964–84. <https://doi.org/10.1021/acsami.2c11953>.

- [19] Wan Y-J, Li X-M, Zhu P-L, Sun R, Wong C-P, Liao W-H. Lightweight, flexible MXene/polymer film with simultaneously excellent mechanical property and high-performance electromagnetic interference shielding. *Compos Part A Appl Sci Manuf* 2020;130:105764. <https://doi.org/10.1016/j.compositesa.2020.105764>.
- [20] Kim S, Lee Y, Park J, So Y, Jung H-T, Ko MJ, Won JC, Jeong S, Kim YH. Green and facile synthesis of hybrid composites with ultralow dielectric properties from water-soluble polyimide and dual-porous silica nanoparticles. *ACS Appl Mater Interfaces* 2023;15:4408–18. <https://doi.org/10.1021/acsami.2c16197>.
- [21] Lee H, Kim D, Kim SH, So Y, Kim YH, Kim J, Park J, Cho JH, Won JC. A water-borne photo-sensitive polyimide precursor for an eco-friendly process of preparing organic thin film transistors. *J Mater Chem C* 2023;11:3459. <https://doi.org/10.1039/D2TC05246F>.
- [22] Ha J, Kim D, Park H, Yoo S, So Y, Kim J, Park J, Won JC, Kim YH. Fabrication of large-area organic thin film transistor array with highly uniform water-borne polyimide gate dielectric via green solvent-engineered bar-coating process. *Adv Electron Mater* 2023;9:2300362. <https://doi.org/10.1002/aelm.202300362>.
- [23] Park S, So Y, Kim KW, Park J, Kim H, Kim LK, Kim J, Jung H-T, Kim DW, Won JC, Kim YH. A novel approach for environmentally benign synthesis and solid-state polymerization of fluorinated polyimides in aqueous co-solvent. *Chem Eng J* 2024;495:153288. <https://doi.org/10.1016/j.cej.2024.153288>.
- [24] Kim D, Kwon YA, So Y, Kim Y-J, Park SW, Park H, Hwang J, Park J, Kim C, Won JC, Cho JH, Kim YH. Water-borne fluorinated polyimide dielectric for large-area IGZO transistors and logic gates. *ACS Appl Mater Interfaces* 2024;16:68328. <https://doi.org/10.1021/acsami.4c14938>.
- [25] So Y, Park J, Ha Y-M, Kim J, Park NK, Kang YY, Lee W, Lee S, Oh SJ, Kwak SJ, Lee WB, Kim Y, Jung H-T, Kim YH, Won JC. Unveiling aqueous polymerization of poly(amic acid) salts for eco-friendly and robust aromatic polyimide structuring. *ACS Sustainable Chem Eng* 2024;12:14747. <https://doi.org/10.1021/acssuschemeng.4c05075>.
- [26] Alhabeb M, Maleski K, Anasori B, Lelyukh P, Clark L, Sin S., gogotsi Y. Guidelines for synthesis and processing of two-dimensional titanium carbide ( $\text{Ti}_3\text{C}_2\text{T}_x$  MXene). *Chem Mater* 2017;29:7633–44. <https://doi.org/10.1021/acs.chemmater.7b02847>.
- [27] Park GS, Ho DH, Lyu B, Jeon S, Ryu DY, Kim DW, Lee N, Kim S, Song YJ, Jo SB, Cho JH. Comb-type polymer-hybridized MXene nanosheets dispersible in arbitrary polar, nonpolar, and ionic solvents. *Sci Adv* 2022;8:eabl5299. <https://doi.org/10.1126/sciadv.abl5299>.
- [28] Jia F, Lu Z, Huang T, Xu M, Xu X, Guo Z, Wang S, Dong J, Kou Y, Hua L. Twin-coated skeleton PEDOT:PSS/MXene/para-aramid nanofibers hybrid aerogel with efficient EMI shielding performance and tunable power coefficient. *Adv Compos Hybrid Mater* 2025;8:200. <https://doi.org/10.1007/s42114-025-01290-5>.
- [29] Du Z, Chen K, Zhang Y, Wang Y, He P, Mi H-Y, Wang Y, Liu C, Shen C. Engineering multilayered MXene/electrospun poly(lactic acid) membrane with increscent electromagnetic interference (EMI) shielding for integrated joule heating and energy generating. *Compos Commun* 2021;26:100770. <https://doi.org/10.1016/j.coco.2021.100770>.
- [30] Zhang F, Ren P, Guo Z, Wang J, Chen Z, Zong Z, Hu J, Jin Y, Ren F. Asymmetric multilayered MXene-AgNWs/cellulose nanofiber composite films with antibacterial properties for high-efficiency electromagnetic interference shielding. *J Mater Sci Technol* 2022;129:181–9. <https://doi.org/10.1016/j.jmst.2022.04.039>.
- [31] Tan Z, Zhao H, Sun F, Ran L, Yi L, Zhao L, Wu J. Fabrication of chitosan/MXene multilayered film based on layer-by-layer assembly: toward enhanced electromagnetic interference shielding and thermal management capacity. *Compos Part A Appl Sci Manuf* 2022;155:106809. <https://doi.org/10.1016/j.compositesa.2022.106809>.
- [32] Jin X, Wang J, Dai L, Liu X, Li L, Yang Y, Cao Y, Wang W, Wu H, Guo S. Flame-retardant poly(vinyl alcohol)/MXene multilayered films with outstanding electromagnetic interference shielding and thermal conductive performances. *Chem Eng J* 2020;380:122475. <https://doi.org/10.1016/j.cej.2019.122475>.
- [33] Feng S, Yi Y, Chen B, Deng P, Zhou Z, Lu C. Rheology-guided assembly of a highly aligned MXene/cellulose nanofiber composite film for high-performance electromagnetic interference shielding and infrared stealth. *ACS Appl Mater Interfaces* 2022;14:36060–70. <https://doi.org/10.1021/acsami.2c11292>.
- [34] Zhou Z, Liu J, Zhang X, Tian D, Zhan Z, Lu C. Ultrathin MXene/calcium alginate aerogel film for high-performance electromagnetic interference shielding. *Adv Mater Interfaces* 2019;6:1802040. <https://doi.org/10.1002/admi.201802040>.
- [35] Cheng Y, Lu Y, Xia M, Piao L, Liu Q, Li M, Zhou Y, Jia K, Yang L, Wang D. Flexible and lightweight MXene/silver nanowire/polyurethane composite foam films for highly efficient electromagnetic interference shielding and photothermal conversion. *Compos Sci Technol* 2021;215:109023. <https://doi.org/10.1016/j.compscitech.2021.109023>.
- [36] Ding R, Yan Q, Xue F, Li P, Xiong J, Zhao X, Liu Z, Xu L, Chen Z, Zheng H, Tang Z, Peng Q, He X. Dual protective porous  $\text{Ti}_3\text{C}_2\text{T}_x$  MXene/polyimide composite film for thermal insulation and electromagnetic interference shielding. *Small* 2023;2023:e2304946. <https://doi.org/10.1002/sml.202304946>.
- [37] Xin W, Ma M-G, Chen F. Silicone-coated MXene/cellulose nanofiber aerogel films with photothermal and joule heating performances for electromagnetic interference shielding. *ACS Appl Nano Mater* 2021;4:7234–43. <https://doi.org/10.1021/acsanm.1c01185>.
- [38] Weng C, Wang G, Dai Z, Pei Y, Liu L, Zhang Z. Buckled AgNW/MXene hybrid hierarchical sponges for high-performance electromagnetic interference shielding. *Nanoscale* 2019;11:22804–12. <https://doi.org/10.1039/c9nr07988b>.
- [39] Li R, Ding L, Gao Q, Zhang H, Zeng D, Zhao B, Fan B, Zhang R. Tuning of anisotropic electrical conductivity and enhancement of EMI shielding of polymer composite foam via  $\text{CO}_2$ -assisted delamination and orientation of MXene. *Chem Eng J* 2021;415:128930. <https://doi.org/10.1016/j.cej.2021.128930>.
- [40] Liang C, Qiu H, Song P, Shi X, Kong J, Gu J. Ultra-light MXene aerogel/wood-derived porous carbon composites with wall-like "mortar/brick" structures for electromagnetic interference shielding. *Sci Bull* 2020;65:616–22. <https://doi.org/10.1016/j.scib.2020.02.009>.
- [41] Rajavel K, Luo S, Wan Y, Yu X, Hu Y, Zhu P, Sun R, Wong C. 2D  $\text{Ti}_3\text{C}_2\text{T}_x$  MXene/polyvinylidene fluoride (PVDF) nanocomposites for attenuation of electromagnetic radiation with excellent heat dissipation. *Compos Part A Appl Sci Manuf* 2020;129:105693. <https://doi.org/10.1016/j.compositesa.2019.105693>.
- [42] Wang L, Chen L, Song P, Liang C, Lu Y, Qiu H, Zhang Y, Kong J, Gu J. *Compos B Eng* 2019;171:111–8. <https://doi.org/10.1016/j.compositesb.2019.05.051>.
- [43] Wang L, Ma Z, Qiu H, Zhang Y, Yu Z, Gu J. Significantly enhanced electromagnetic interference shielding performances of epoxy nanocomposites with long-range aligned lamellar structures. *Nano-Micro Lett* 2022;14:224. <https://doi.org/10.1007/s40820-022-00949-8>.
- [44] Cao H, Escamilla M, Anas M, Tan Z, Gulati S, Yun J, Arolo KD, Lutkenhaus JL, Radovic M, Pentzer EB, Green MJ. Synthesis and electronic applications of particle-templated  $\text{Ti}_3\text{C}_2\text{T}_x$  MXene-polymer films via pickering emulsion polymerization. *ACS Appl Mater Interfaces* 2021;13:51556–66. <https://doi.org/10.1021/acsami.1c16234>.
- [45] Sun R, Zhang HB, Liu J, Xie X, Yang R, Li Y, Hong S, Yu ZZ. Highly conductive transition metal carbide/carbonitride (MXene)/polystyrene nanocomposites fabricated by electrostatic assembly for highly efficient electromagnetic interference shielding. *Adv Funct Mater* 2017;27:1702807. <https://doi.org/10.1002/adfm.201702807>.